

ASOCEM: Automatic Segmentation Of Contaminations in cryo-EM

Amitay Eldar*, Ido Amos, Yoel Shkolnisky

Department of Applied Mathematics, School of Mathematical Sciences, Tel-Aviv University, Tel-Aviv, Israel

Abstract

Particle picking is currently a critical step in the cryo-electron microscopy single particle reconstruction pipeline. Contaminations in the acquired micrographs severely degrade the performance of particle pickers, resulting in many “non-particles” in the collected stack of particles. In this paper, we present ASOCEM (Automatic Segmentation Of Contaminations in cryo-EM), an automatic method to detect and segment contaminations, which requires as an input only the approximated particle size. In particular, it does not require any parameter tuning nor manual intervention. Our method is based on the observation that the statistical distribution of contaminated regions is different from that of the rest of the micrograph. This nonrestrictive assumption allows to automatically detect various types of contaminations, from the carbon edges of the supporting grid to high contrast blobs of different sizes. We demonstrate the efficiency of our algorithm using various experimental data sets containing various types of contaminations. ASOCEM is integrated as part of the KLT picker [6] and is available at <https://github.com/ShkolniskyLab/kltpicker2>.

1. Introduction

Single particle cryo-electron microscopy (cryo-EM) is an established method for high resolution structure determination of macro-molecules. A typical cryo-EM data set consists of hundreds of noisy images, called micrographs, with each micrograph containing multiple two-dimensional particle images (that are essentially two-dimensional tomographic projections of the investigated macro-molecule). In order to determine a high resolution three-dimensional model of the macro-molecule, one needs many thousands of particle images, to overcome their high level of noise. Therefore, one of the first steps towards three-dimensional reconstruction is detecting and segmenting the particles images from the micrographs, a step known as “particle picking” [16].

Typical micrographs consist of three types of regions – regions of particles with added noise, regions of noise only, and regions of contaminations. The latter can cause various problems to existing particle picking algorithms, from high rate of false-positives (picking “non-particles”) to completely breaking down the picking process. Over the past few years, two main approaches were developed to address the problem of contami-

nations in cryo-EM data. The first approach combines contamination detection within the picking process. For pickers based on deep learning, this means including labeled contaminated data as part of the training process [19, 20, 22, 17]. Other pickers use morphological operators to avoid contaminations [9, 12]. The second approach separates the task of contamination detection from the picking step. In this approach, one first detects the contaminated regions, and then uses this information (typically in the form of a binary mask) as an input to an existing particle picking algorithm, which has been adapted to skip the contaminated regions. Representatives for this approach include EMHP [2], which is designed to detect only carbon contaminations through edge detection methods based on Sobel filtering, and MicrographCleaner [14], which is a deep learning based algorithm that uses a U-net trained on a data set of 539 manually segmented micrographs.

In this paper, we present ASOCEM: Automatic Segmentation Of Contaminations in cryo-EM, whose only required parameter is the estimated particle size. Our approach is based on the assumption that the contaminated and uncontaminated regions are Gaussian processes with different and unknown means and covariances. In other words, contaminated and uncontaminated regions have different statistics. This nonrestrictive assumption allows to detect various types of contaminations, as demonstrated in Section 3. We note that our algorithm is also

*Corresponding author

Email addresses: amitayeldar@tauex.tau.ac.il (Amitay Eldar), idoamos@mail.tau.ac.il (Ido Amos), yoelsh@tauex.tau.ac.il (Yoel Shkolnisky)

applicable to micrographs with no contaminations, provided the user allows for a low percentage of false positives (that is, uncontaminated regions that are being detected as contaminations). Our algorithm requires a few seconds per micrograph, and returns for each micrograph a binary mask indicating the locations of contaminations that should be excluded by subsequent particle picking. An implementation of our algorithm has been integrated into the KLT picker [6], allowing the user to detect contamination (the outputs are binary masks), and also perform particle picking directly from contaminated micrographs. The enhanced KLT picker is available at <https://github.com/ShkolniskyLab/kltpicker2>.

2. Materials and methods

We model a micrograph as a random discrete function $I : G \rightarrow \mathbb{R}$, where $G \subset [0, 1]^2$ is a two-dimensional evenly-spaced grid. We denote by \mathcal{G} a partition of the unit square, that is $\mathcal{G} = (\mathcal{G}_0, \mathcal{G}_1)$ such that $\mathcal{G}_0 \cap \mathcal{G}_1 = \emptyset$ and $\mathcal{G}_0 \cup \mathcal{G}_1 = [0, 1]^2$. In this notation, \mathcal{G}_0 represents the contaminated region and \mathcal{G}_1 the uncontaminated region of the micrograph. Note that we use only two types of regions, as a finer partition requires a more complicated model planned as a future research. Denote $G_0 = G \cap \mathcal{G}_0$, $G_1 = G \cap \mathcal{G}_1$, and assume that $I|_{G_0} \sim \mathcal{N}(\mu_0, \Sigma_0)$, $I|_{G_1} \sim \mathcal{N}(\mu_1, \Sigma_1)$, where $\mathcal{N}(\mu, \Sigma)$ is a normal distribution with mean μ and covariance Σ . Moreover, assume that $I|_{G_0}$ and $I|_{G_1}$ are independent and stationary (stationary means that for any two points $x, y \in G_i$, $i = 1, 2$, the covariance $\Sigma_i(x, y)$ depends only on $x - y$). Given this model, the problem of segmenting a micrograph into “good” and “bad” regions is stated as follows: estimate \mathcal{G} given a realization of I , where the parameters $\mu_0, \Sigma_0, \mu_1, \Sigma_1$ are unknown. In practice, a “realization of I ” is simply the input micrograph. We note that as both regions $\mathcal{G}_0, \mathcal{G}_1$ are represented by Gaussian processes with unknown parameters, one can’t determine, without making further assumptions, which one represents the contaminated region. To address this problem, we will assume that the contaminated region has smaller area. In order to estimate \mathcal{G} , we maximize the likelihood function $\mathcal{L}(\Theta|I) := f_I(G; \Theta)$ where f_I is the probability density of I (to be defined shortly) and $\Theta = (\mathcal{G}, \mu_0, \Sigma_0, \mu_1, \Sigma_1)$. One can show that if the partition \mathcal{G} is not “nice” enough, for example if the boundary of \mathcal{G}_0 is not smooth or with infinite length, then this maximization problem is ill posed and needs to be regularized [4]. We choose a regularization term based on the assumption that the contaminated

area and its boundary are not too large, which yields the maximization problem

$$\hat{\Theta} = \arg \max_{\Theta} f_I(G; \Theta) \cdot e^{-(\alpha \cdot \text{Length}(\partial \mathcal{G}_0) + \beta \cdot \text{Area}(\mathcal{G}_0))}, \quad (1)$$

where on the right hand side, the left term is the above-mentioned likelihood, the right term is the regularization term with $\partial \mathcal{G}_0$ being the boundary of \mathcal{G}_0 , and α, β are positive parameters. The mathematical model described in this section (up to equation (1)), is a generalization of the well known Chan-Vese model [4] to the case where the contaminated and uncontaminated regions are assumed to be Gaussian processes with different and unknown mean and covariance. Contrary to our generalization, the classical Chan-Vese model assumes different means and variances, but without any correlations between different points in space. A common approach to estimate the solution of (1) is by alternating maximization, where in each iteration we estimate the solution with respect to one variable while treating the others as constants. Thus, we first treat \mathcal{G} as constant and estimate the statistical parameters $\mu_0, \Sigma_0, \mu_1, \Sigma_1$. Since we have only one realization of I (our input micrograph), we can’t estimate the statistical parameters without making further assumptions. A common assumption in cryo-EM is that the correlation between pixels decays fast as the distance between them grows. To take advantage of this assumption, we partition $[0, 1]^2$ into N non-overlapping squares \mathcal{B}_i , and assume for simplicity that all squares have the same area \mathcal{B} . Denote $B_i = \mathcal{B}_i \cap G$, and assume that pixels from different squares are independent, which implies that for all B_i and B_j ,

$$(f_I)|_{B_i \cup B_j} = (f_I)|_{B_i} \cdot (f_I)|_{B_j}. \quad (2)$$

Since $I|_{G_0}$ is stationary, for each $B_i, B_j \subset G_0$ we have that $\Sigma_0|_{B_i} = \Sigma_0|_{B_j}$, which we denote by $\Sigma_0^B := \Sigma_0|_{B_i}$. The latter implies that the density of pixel intensities of I on each $B_i \subset G_0$ can be written as

$$\rho_{B_i}^0 := f_I|_{B_i} = \frac{\exp\left(-\frac{1}{2}(x_{B_i} - \mu_0)^T (\Sigma_0^B)^{-1} (x_{B_i} - \mu_0)\right)}{\sqrt{(2\pi)^n \det \Sigma_0^B}},$$

where $x_{B_i} \in \mathbb{R}^n$ is the column stack vector of B_i . For $I|_{G_1}$ we define $\rho_{B_i}^1$ in a similar way. Next, denote

$$f_{B_i}^0 = \begin{cases} \rho_{B_i}^0 & B_i \cap G_0 \neq \emptyset, \\ 1 & \text{otherwise,} \end{cases} \quad (3)$$

then, by ignoring the error induced by boxes \mathcal{B}_i on the boundary of \mathcal{G}_0 and using (2), we have that

$$f_{I|G_0} = \prod_{i=1}^N f_{B_i}^0. \quad (4)$$

The same derivation for \mathcal{G}_1 yields $f_{I|G_1} = \prod_{i=1}^N f_{B_i}^1$, where $f_{B_i}^1$ is defined similarly to (3) but on G_1 . As mentioned above, $I|_{G_0}$ and $I|_{G_1}$ are independent, and therefore, using (4) we get that f_I from (1) is given by

$$f_I = f_{I|G_0} \cdot f_{I|G_1} = \prod_{i=1}^N f_{B_i}^0 \cdot \prod_{j=1}^N f_{B_j}^1.$$

Substituting the latter equation back into (1) and taking the logarithm gives

$$\hat{\Theta} = \arg \max_{\Theta} \sum_{i=1}^N \log f_{B_i}^0 + \sum_{j=1}^N \log f_{B_j}^1 - (\alpha \cdot \text{Length}(\partial \mathcal{G}_0) + \beta \cdot \text{Area}(\mathcal{G}_0)). \quad (5)$$

By differentiating (5) with respect to μ_0 and Σ_0^B and equating to zero, we get that these parameters can be estimated as the sample mean and sample covariance of $\{x_{B_i} | B_i \cap G_0 \neq \emptyset\}$ (see [1] for more details). The parameters μ_1, Σ_1^B are estimated similarly.

Next, treating $\mu_0, \Sigma_0^B, \mu_1, \Sigma_1^B$ as constants, we turn to estimating \mathcal{G} , which is the partition of the unit square to the contaminated and uncontaminated regions. Inspired by the level set method of Chan-Vese [4], instead of estimating \mathcal{G} , we estimate a level set Lipschitz function $\varphi : [0, 1]^2 \rightarrow \mathbb{R}$ such that $\{\varphi > 0\} = \mathcal{G}_0$, $\{\varphi < 0\} = \mathcal{G}_1$, $\{\varphi = 0\} = \partial \mathcal{G}_0$. To that end, we rewrite (5) as an integral maximization problem as follows. Using the Heaviside step function

$$H(x) = \begin{cases} 1 & x > 0, \\ 0 & \text{otherwise,} \end{cases} \quad (6)$$

and its derivative the Dirac δ function, it holds that

$$\begin{aligned} \text{Area}(\mathcal{G}_0) &= \int_{[0,1]^2} H(\varphi(x)) dx, \\ \text{Length}(\partial \mathcal{G}_0) &= \int_{[0,1]^2} \delta(\varphi(x)) \|\nabla \varphi(x)\| dx. \end{aligned} \quad (7)$$

In addition, for every $B_i \subset G_0$ or $B_i \cap G_0 = \emptyset$, it follows from

the definition of $f_{B_i}^0$ (see (3)) that

$$\log f_{B_i}^0 = \frac{1}{\mathcal{B}} \int_{[0,1]^2} \log f_{B_i}^0 \cdot \mathbb{1}_{B_i}(x) \cdot H(\varphi(x)) dx,$$

where $\mathbb{1}_{B_i}$ is the indicator function of the set B_i . Similarly, for every $B_i \subset G_1$ or $B_i \cap G_1 = \emptyset$

$$\log f_{B_i}^1 = \frac{1}{\mathcal{B}} \int_{[0,1]^2} \log f_{B_i}^1 \cdot \mathbb{1}_{B_i}(x) \cdot (1 - H(\varphi(x))) dx.$$

By ignoring as above the error induced by boxes \mathcal{B}_i on the boundary of \mathcal{G}_0 , the latter two equations imply that the sums of the logarithms in (5) can be written as

$$\begin{aligned} \sum_{i=1}^N \log f_{B_i}^0 &= \frac{1}{\mathcal{B}} \int_{[0,1]^2} \sum_{i=1}^N \log f_{B_i}^0 \cdot \mathbb{1}_{B_i}(x) \cdot H(\varphi(x)) dx, \\ \sum_{i=1}^N \log f_{B_i}^1 &= \frac{1}{\mathcal{B}} \int_{[0,1]^2} \sum_{i=1}^N \log f_{B_i}^1 \cdot \mathbb{1}_{B_i}(x) \cdot (1 - H(\varphi(x))) dx. \end{aligned} \quad (8)$$

Using (7), (8) and the notation

$$g_0(x) = \sum_{i=1}^N \log f_{B_i}^0 \cdot \mathbb{1}_{B_i}(x), \quad g_1(x) = \sum_{i=1}^N \log f_{B_i}^1 \cdot \mathbb{1}_{B_i}(x),$$

and recalling that $\mu_0, \Sigma_0^B, \mu_1, \Sigma_1^B$ are fixed, the optimization problem (5) becomes

$$\hat{\varphi} = \arg \max_{\Theta} \frac{1}{\mathcal{B}} \int_{[0,1]^2} g_0(x) H(\varphi(x)) + g_1(x) (1 - H(\varphi(x))) - \beta \mathcal{B} \cdot H(\varphi(x)) - \alpha \mathcal{B} \cdot \delta(\varphi(x)) \|\nabla \varphi(x)\| dx. \quad (9)$$

Using calculus of variations, we show in Appendix A that the solution $\hat{\varphi}$ of the latter optimization problem is given as the limit $\hat{\varphi}(x) = \lim_{t \rightarrow \infty} \bar{\varphi}(x, t)$, where $\bar{\varphi}(x, t)$ is the solution of the differential equation

$$\bar{\varphi}_t = \delta_a(\bar{\varphi}) \cdot \left[-\alpha \cdot \text{div} \left(\frac{\nabla \bar{\varphi}}{\|\nabla \bar{\varphi}\|} \right) - \beta + \frac{1}{\mathcal{B}} \sum_{i=1}^N \mathbb{1}_{B_i} \log \left(\frac{f_{B_i}^0}{f_{B_i}^1} \right) \right], \quad (10)$$

with δ_a being a smooth function which converges to the Dirac δ function when $a \rightarrow 0$ (see Appendix (A.9) for details). We estimate the solution of (10) using a finite difference scheme as proposed in [4].

3. Experimental results

In this section, we demonstrate the performance of our ASOCM algorithm on various data sets. We also demonstrate that integrating the algorithm with the KLT picker [6] improves particle

picking results. We compare the performance of our algorithm to that of MicrographCleaner [14] as both algorithms are fully automatic and only require as a parameter an estimate of the particle size (with MicrographCleaner we used the default detection threshold of 0.2). The performance measures we report for the algorithms are sensitivity and specificity [7]. In our settings, sensitivity is the ratio between the number of pixels an algorithm detects as contamination and the total number of pixels labeled as contamination. Specificity is the ratio between the number of pixels detected by the algorithm as uncontaminated and the total number of uncontaminated pixels in the micrograph. We would like both sensitivity and specificity to be as close to one as possible. We tested our algorithm using three data sets, described in detail below. The first data set was provided by the MicrographCleaner team, and was used as part of the MicrographCleaner training data. The two other data sets were annotated by our team. The main difference between the first data set and the other two is that the latter have not been used in the training process of MicrographCleaner, and therefore, provide more objective performance measures.

Finally we demonstrate how ASOCCEM may improve the picking results of the KLT picker [6]. It is worth noting that the popular RELION [15] and EMAN [13] particle pickers do not support the use of contamination masks, so we cannot use them to demonstrate the benefits of ASOCCEM.

3.1. MicrographCleaner data

The MicrographCleaner data set consists of 111 micrographs, of different sizes and with various contaminations, extracted from 12 different cryo-EM data sets. These micrographs were used in the training process of the MicrographCleaner algorithm. The ground-truth for this data set was generated by manual annotation by the MicrographCleaner team. Table 1 presents the average performance measures for each of the data sets. Figure 2 shows 3 micrographs and the detection results of ASOCCEM and MicrographCleaner.

3.2. Untrained data

This test data consists of 13 micrographs with various contaminations, extracted from 3 different cryo-EM data sets [5, 10, 3], 8 micrograph from the first data set, 3 from the second and 2 from the third. The ground truth for this test data was generated by manual annotation. All micrographs were downsampled to size 800×800 pixels prior to contamination detection. Table 3 shows the average performance measures for these test

data. Figure 4 shows 3 micrographs (one from each data set) and the detection results of ASOCCEM and MicrographCleaner.

3.3. Integrating ASOCCEM with the KLT picker

In this section, we demonstrate that integrating contamination detection with particle picking may improve the results of the picking. To demonstrate this point, we compare between the performance of the KLT picker [6] and an enhanced version of the KLT picker into which the ASOCCEM algorithm has been integrated. In the enhanced KLT picker, the ASOCCEM algorithm first detects all contaminated pixels, and then the KLT picker ignores these pixels during picking. The KLT picker with integrated ASOCCEM algorithm is available at <https://github.com/ShkolniskyLab/kltpicker2>. To compare both versions of the KLT picker we use micrographs from the Plasmodium falciparum 80S ribosome data set [21]. Figure 5 shows a micrograph for which the KLT picker is picking contaminated pixels as particles, but still manages to pick “good” particles as well. The micrograph in Figure 6 shows a worse and more common case where contamination results in failure of the picking process. In both cases, the picking results of the enhanced algorithm are much better.

4. Discussion

Before comparing the detection results of ASOCCEM and MicrographCleaner, it is important to note that the latter allows the user to tune the detection threshold of the algorithm. Nevertheless, we used the default threshold of 0.2 in all experiments. In some data sets, changing the threshold may improve the results, however, as noted in [14], the cryo-EM field is moving towards streaming and automatic processing, and thus, default parameters should perform decently in most cases. As of running times, both algorithms have comparable running times, of about a few seconds per micrograph.

4.1. MicrographCleaner data

It is not surprising that for this data MicrographCleaner often slightly outperforms ASOCCEM, as this data was used to train the MicrographCleaner algorithm. The sensitivity results of both algorithms are very similar, but MicrographCleaner has slightly better specificity scores (though both algorithms yield very high scores). From the user’s perspective, this means that both algorithms will detect the same high percentage of contaminations, while ASOCCEM leaves slightly less data for subsequent particle picking. It is important to note that all mi-

crographs in this data set are only available after being down-sampled by the MicrographCleaner team to size of about 400×400 pixels. Such sizes are sub-optimal for the ASOCCEM algorithm that performs best when the micrographs are at least of size 600×600 pixels. The reason ASOCCEM benefits from larger micrographs is due to the covariances estimation step (see the paragraph below equation (1)). In this step, the contaminated and uncontaminated regions are being divided into non-overlapping boxes of the same size, which are being used to approximate the covariance of each region. In practice, each box is of size 25×25 pixels and one needs enough of them in order to get a good approximation. As the number of boxes depends on the area of the contamination, it seems that downsampling the micrograph to less than 600×600 pixels is sub-optimal in most cases.

4.2. Untrained data

This data best represents a fair comparison between ASOCCEM and MicrographCleaner, as it contains micrographs which have not been used to train the MicrographCleaner algorithm. The results of both algorithms are comparable, with a slight advantage to ASOCCEM on the sensitivity measure, and a slight advantage to MicrographCleaner on the specificity measure.

5. Conclusion

In this paper, we presented ASOCCEM, an automatic algorithm for detecting contaminations in cryo-EM micrographs. The algorithm is inspired by the well known Chan-Vese algorithm and is based on a general statistical model that allows it to detect various types of contaminations. To demonstrate the performance of our algorithm, we tested ASOCCEM on various data sets, showing performance that is comparable to that of MicrographCleaner, but without requiring any training, which is labor-intensive as it requires to manually annotate contaminations in a large set of micrographs.

The ASOCCEM algorithm partitions the micrographs into two regions: contaminated and uncontaminated. This partition is necessarily sub-optimal, as it may happen that the statistical properties of particle regions resemble more to those of contamination regions than to those of noise-only regions. In such cases, particles would be classified as contaminations. ASOCCEM alleviates this problem by computing the area of each region marked as contamination and keeping only those regions whose areas are significantly larger than the particle size. In fact, this is the only place where the particle size is used

Data set	Sensitivity		Specificity	
	ASOCCEM	Micrograph Cleaner	ASOCCEM	Micrograph Cleaner
10005	0.94	0.92	0.94	0.99
10028	0.91	0.94	0.97	0.99
10190	0.84	0.82	0.92	0.99
10033	0.94	0.95	0.97	0.99
10077	0.83	0.72	0.95	0.99
10081	0.73	0.75	0.97	0.99
10097	0.84	0.93	0.95	0.99
10099	0.79	0.83	0.91	0.99
10168	0.73	0.84	0.92	1.00
10175	0.84	0.90	0.98	1.00
10205	0.84	0.76	0.95	0.99
10217	0.57	0.93	0.89	0.89

Figure 1: Average performance using the MicrographCleaner training data set. The data set consists of 111 micrographs of different sizes and with various contaminations, extracted from 12 cryo-EM data sets from the EMPIAR repository [11]. The names of the data sets are given in the left column.

by the algorithm. A better approach would be to partition the micrographs into three different regions: contaminations, particle plus noise, and noise only. This approach will eliminate the need to provide the algorithm with the approximate particle size, turning the algorithm into completely parameter free.

Acknowledgments

This research was supported by the European Research Council (ERC) under the European Union’s Horizon 2020 research and innovation programme (grant agreement 723991 - CRY-OMATH).

Appendix A. Deriving the solution of (9)

Denoting

$$F(\varphi) = \frac{1}{\mathcal{B}} \int_{[0,1]^2} g_0(x)H(\varphi(x)) + g_1(x)(1 - H(\varphi(x))) - \beta \mathcal{B} \cdot H(\varphi(x)) - \alpha \mathcal{B} \cdot \delta(\varphi(x)) \|\nabla \varphi(x)\| dx, \quad (\text{A.1})$$

equation (9) becomes

$$\hat{\varphi} = \arg \max_{\varphi} F(\varphi), \quad (\text{A.2})$$

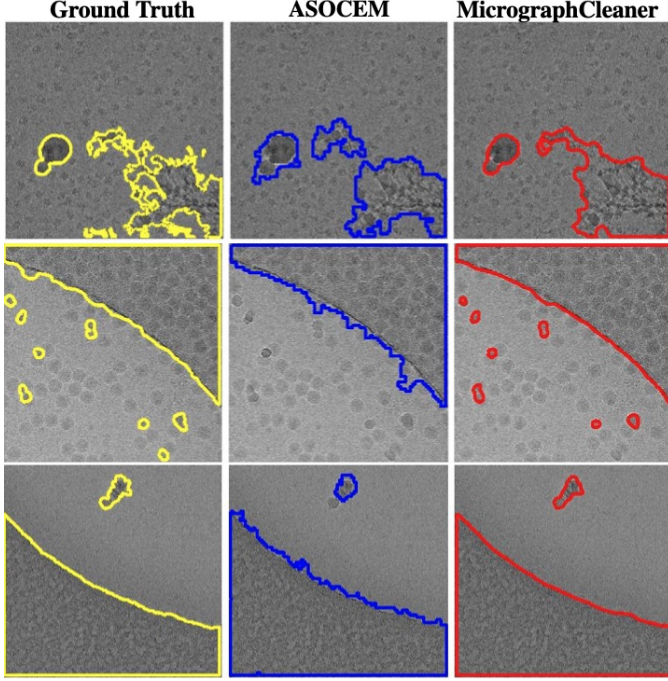


Figure 2: Examples of detection results for 3 micrographs from the MicrographCleaner data set for both ASOCCEM (middle column) and MicrographCleaner (right column). Manually annotated ground-truth is shown on the left column.

Data set	Sensitivity		Specificity	
	ASOCCEM	Micrograph Cleaner	ASOCCEM	Micrograph Cleaner
FerritinM6A	0.83	0.84	0.99	0.99
ESRF0919	0.98	0.98	0.85	0.98
ESRF1118	0.76	0.71	0.96	0.99

Figure 3: Average performance for the untrained data set. This data set consists of 13 micrographs, which were extracted from 3 different cryo-EM data sets [5, 10, 3].

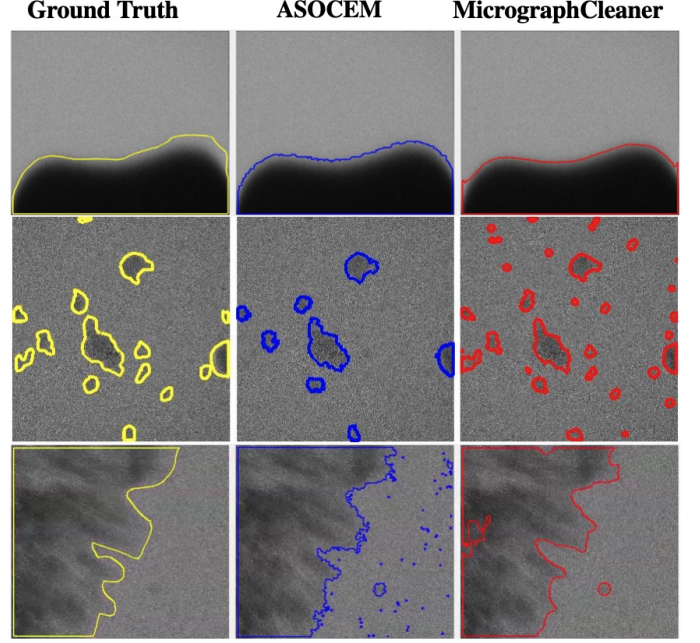


Figure 4: Examples of detection results for 3 micrographs from the untrained data set for both ASOCCEM (middle column) and MicrographCleaner (right column). Manually annotated ground-truth is shown on the left column. The top-to-bottom micrographs were taken, by the same order, from the following cryo-EM data sets [5, 10, 3].

where φ is a Lipschitz function. In [18, p.45], it is shown that the optimum $\hat{\varphi}$ of (A.2) is given as the limit $\hat{\varphi}(x) = \lim_{t \rightarrow \infty} \bar{\varphi}(x, t)$, where $\bar{\varphi}(x, t)$ is the solution of the gradient descent equations

$$\begin{aligned} \frac{d\bar{\varphi}}{dt} &= \frac{dF}{d\bar{\varphi}} \\ \bar{\varphi}(0, x) &= \bar{\varphi}_0(x) \\ \frac{\delta(\bar{\varphi})}{\|\nabla \bar{\varphi}\|} \cdot \frac{\partial \bar{\varphi}}{\partial \vec{n}} &= 0 \text{ on } \partial([0, 1]^2), \end{aligned} \quad (\text{A.3})$$

where $\frac{dF}{d\bar{\varphi}}$ is the functional derivative [8, p.27], $\bar{\varphi}_0(x)$ is an initial condition (in our case we used a spherical cap $\bar{\varphi}_0(x, y) = 0.25 - ((x - 0.5)^2 + (y - 0.5)^2)$), and $\frac{\partial}{\partial \vec{n}}$ is the normal derivative with respect to the boundary of $[0, 1]^2$. It is well known that $\frac{dF}{d\bar{\varphi}}$ can be deduced from the total derivative $\frac{d}{d\epsilon} \Big|_{\epsilon=0} F(\bar{\varphi} + \epsilon \cdot u)$ [8, p.14], where ϵ is a real number and $u : [0, 1]^2 \rightarrow \mathbb{R}$ is an arbitrary Lipschitz function with the same boundary condition as $\bar{\varphi}$, namely $\frac{\delta(u)}{\|\nabla u\|} \cdot \frac{\partial u}{\partial \vec{n}} = 0$. Therefore, to compute $\frac{dF}{d\bar{\varphi}}$ we turn to compute $\frac{d}{d\epsilon} \Big|_{\epsilon=0} F(\bar{\varphi} + \epsilon \cdot u)$. As $\frac{d}{d\epsilon} \Big|_{\epsilon=0}$ is a linear operator, we can differentiate each of the terms in $F(\bar{\varphi})$ separately. The first

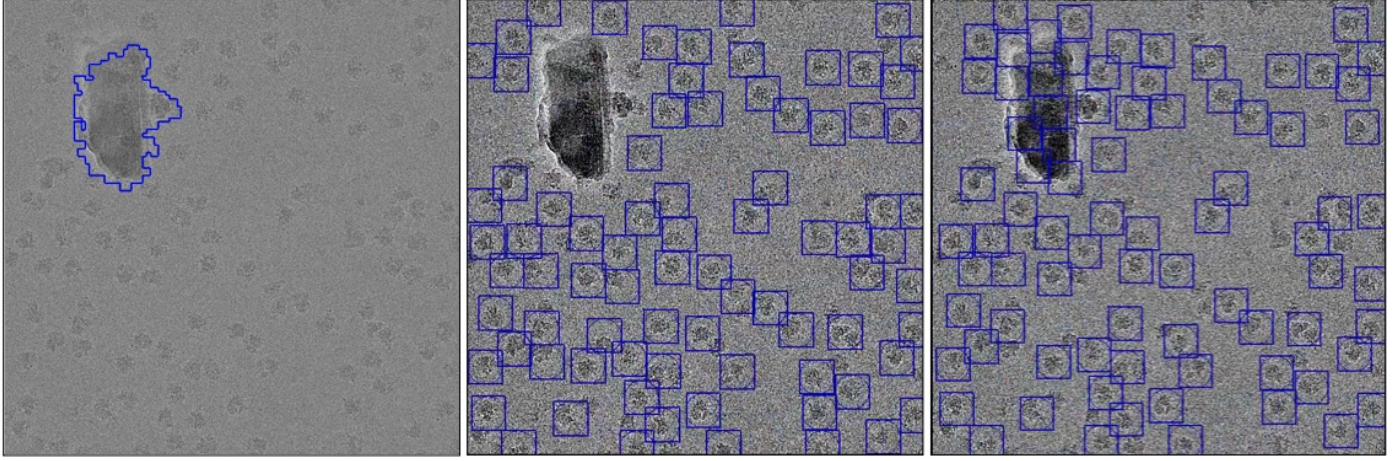


Figure 5: Integrating contamination detection with particle picking. Left column shows the contamination detected by the ASOCCEM algorithm. Middle column shows the picking results when combining the ASOCCEM algorithm with the KLT picker [6]. Right column shows the picking results of the KLT picker when ignoring the presence of contaminations. This example demonstrates the case where the KLT picker is picking contaminated data as particles, but still manages to pick "good" particles as well. The micrograph in this example is part of the *Plasmodium falciparum* 80S ribosome data set [21].

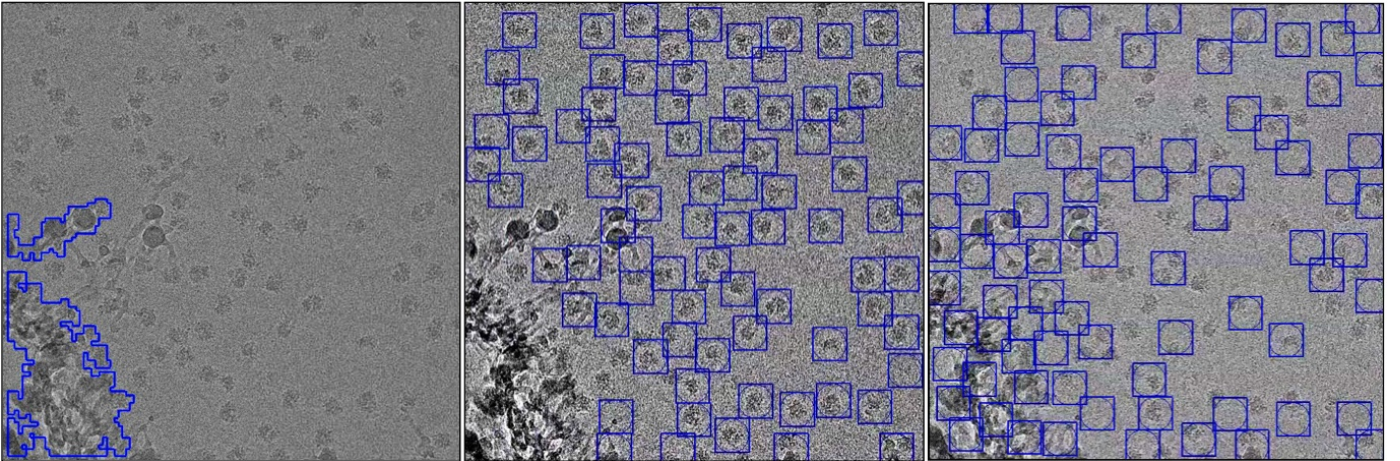


Figure 6: Same experiment as in Figure 5 but for a different micrograph. For this micrograph, ignoring the presence of contaminations during particle picking results in failure of the particle picking algorithm. The micrograph in this example is part of the *Plasmodium falciparum* 80S ribosome data set [21].

term is

$$\begin{aligned}
& \left. \frac{d}{d\epsilon} \right|_{\epsilon=0} \frac{1}{\mathcal{B}} \int_{[0,1]^2} g_0(x) H(\bar{\varphi}(x) + \epsilon \cdot u(x)) dx \\
&= \frac{1}{\mathcal{B}} \int_{[0,1]^2} g_0(x) \left. \frac{d}{d\epsilon} \right|_{\epsilon=0} H(\bar{\varphi}(x) + \epsilon \cdot u(x)) dx \\
&= \frac{1}{\mathcal{B}} \int_{[0,1]^2} g_0(x) \delta(\bar{\varphi}(x)) u(x) dx. \tag{A.4}
\end{aligned}$$

For simplicity, in subsequent derivations, we drop the dependence on x . The second term is

$$\begin{aligned}
& \left. \frac{d}{d\epsilon} \right|_{\epsilon=0} \frac{1}{\mathcal{B}} \int_{[0,1]^2} g_1 \left(1 - H(\bar{\varphi} + \epsilon \cdot u) \right) dx \\
&= \frac{1}{\mathcal{B}} \int_{[0,1]^2} g_1 \left. \frac{d}{d\epsilon} \right|_{\epsilon=0} \left(1 - H(\bar{\varphi} + \epsilon \cdot u) \right) dx \\
&= -\frac{1}{\mathcal{B}} \int_{[0,1]^2} g_1 \delta(\bar{\varphi}) u dx. \tag{A.5}
\end{aligned}$$

The third term is

$$\begin{aligned}
& \left. \frac{d}{d\epsilon} \right|_{\epsilon=0} - \int_{[0,1]^2} \beta \cdot H(\bar{\varphi} + \epsilon \cdot u) dx \\
&= - \int_{[0,1]^2} \beta \cdot \left. \frac{d}{d\epsilon} \right|_{\epsilon=0} H(\bar{\varphi} + \epsilon \cdot u) dx \\
&= - \int_{[0,1]^2} \beta \cdot \delta(\bar{\varphi}) u dx. \tag{A.6}
\end{aligned}$$

Finally, the forth term is

$$\begin{aligned}
& \left. \frac{d}{d\epsilon} \right|_{\epsilon=0} - \int_{[0,1]^2} \alpha \cdot \delta(\bar{\varphi} + \epsilon \cdot u) \|\nabla \bar{\varphi} + \epsilon \cdot u\| dx \\
&= - \int_{[0,1]^2} \alpha \cdot \left. \frac{d}{d\epsilon} \right|_{\epsilon=0} \delta(\bar{\varphi} + \epsilon \cdot u) \cdot \|\nabla \bar{\varphi} + \epsilon \cdot u\| dx \\
&= - \int_{[0,1]^2} \alpha \delta(\bar{\varphi}) \cdot \operatorname{div} \left(\frac{\nabla \bar{\varphi}}{\|\nabla \bar{\varphi}\|} \right) u dx, \tag{A.7}
\end{aligned}$$

where the last step (A.7) involves basic differential calculus, similar to the one in [4] (we omit the calculations for the sake of brevity). The desired functional derivative is equal to the integrand of the sum of (A.4)–(A.7) after dropping the multiplication by $u(x)$, that is

$$\frac{dF}{d\bar{\varphi}} = \delta(\bar{\varphi}) \cdot \left[-\alpha \cdot \operatorname{div} \left(\frac{\nabla \bar{\varphi}}{\|\nabla \bar{\varphi}\|} \right) - \beta + \frac{1}{\mathcal{B}} \sum_{i=1}^N \mathbb{1}_{\mathcal{B}_i} \log \left(\frac{f_{\mathcal{B}_i}^0}{f_{\mathcal{B}_i}^1} \right) \right]. \tag{A.8}$$

In order to estimate the solution of (A.3), we follow Chan-Vese method [4], and replace H and δ by their regularized versions

$$\begin{aligned}
H_a(z) &= \frac{1}{2} \left(1 + \frac{2}{\pi} \arctan(za^{-1}) \right), \\
\delta_a(z) &= \frac{d}{dz} H_a(z) = \frac{a}{\pi(a^2 + z^2)},
\end{aligned} \tag{A.9}$$

which means practically replacing δ with δ_a in (A.8). Then, we use the same finite differences scheme and the same parameters $a = dt = 1$ as in [4] to estimate the solution of the differential equation (A.3).

References

- [1] T. W. Anderson and I. Olkin. Maximum-likelihood estimation of the parameters of a multivariate normal distribution. *Linear Algebra and its Applications*, 70:147–171, 1985.
- [2] Zachary Berendsen, Charles Bowman, Haerin Jang, and Andrew B. Ward. EMHP: an accurate automated hole masking algorithm for single-particle cryo-EM image processing. *Bioinformatics*, 33(23):3824–3826, 08 2017.
- [3] Ido Caspy, Tirupathi Malavath, Daniel Klaiman, Maria Fadeeva, Yoel Shkolnisky, and Nathan Nelson. Structure and energy transfer pathways of the dunaliella salina photosystem i supercomplex. *Biochimica et Biophysica Acta (BBA) - Bioenergetics*, 1861(10):148253, 2020.
- [4] T. F. Chan and L. A. Vese. Active contours without edges. *IEEE Transactions on Image Processing*, 10(2):266–277, 2001.
- [5] Geula Davidov, Gili Abelya, Ran Zalk, Benjamin Izicki, Sharon Shaibi, Lior Spektor, Dayana Shagidov, Esther G. Meyron-Holtz, Raz Zarivach, and Gabriel A. Frank. Folding of an intrinsically disordered iron-binding peptide in response to sedimentation revealed by cryo-em. *Journal of the American Chemical Society*, 142(46):19551–19557, 11 2020.
- [6] Amitay Eldar, Boris Landa, and Yoel Shkolnisky. Klt picker: Particle picking using data-driven optimal templates. *Journal of Structural Biology*, 210(2):107473, 2020.
- [7] Gary M. Gaddis and Monica L. Gaddis. Introduction to biostatistics: Part 3, sensitivity, specificity, predictive value, and hypothesis testing. *Annals of Emergency Medicine*, 19(5):591–597, 1990.
- [8] I. M. Gelfand. *Calculus of Variations*. Dover Publications, 2012.
- [9] Ayelet Heimowitz, Joakim Andén, and Amit Singer. Apple picker: Automatic particle picking, a low-effort cryo-em framework. *Journal of Structural Biology*, 204(2):215–227, 2018.
- [10] Michael Hippler and Nathan Nelson. The Plasticity of Photosystem I. *Plant and Cell Physiology*, 62(7):1073–1081, 2021.
- [11] Andrii Iudin, Paul K. Korir, José Salavert-Torres, Gerard J. Kleywegt, and Ardan Patwardhan. Empiar: a public archive for raw electron microscopy image data. *Nature Methods*, 13(5):387–388, 2016.
- [12] Robert Langlois, Jesper Pallesen, Jordan T. Ash, Danny Nam Ho, John L. Rubinstein, and Joachim Frank. Automated particle picking for low-contrast macromolecules in cryo-electron microscopy. *Journal of Structural Biology*, 186(1):1–7, 2014.
- [13] Steven Ludtke, Philip Baldwin, and Wah Chiu. Eman: semi automated software for high-resolution single-particle reconstructions. *Journal of structural biology*, 128:82–97, 01 2000.
- [14] Ruben Sanchez-Garcia, Joan Segura, David Maluenda, C. O. S. Sorzano, and J. M. Carazo. Micrographcleaner: A python package for cryo-em

- micrograph cleaning using deep learning. *Journal of Structural Biology*, 210(3):107498, 2020.
- [15] Sjors HW Scheres. Semi-automated selection of cryo-em particles in relion 1.3. *Journal of structural biology*, 189(2):114–122, 2015.
 - [16] Amit Singer and Fred J. Sigworth. Computational methods for single-particle electron cryomicroscopy. *Annual Review of Biomedical Data Science*, 3:163–190, 2020.
 - [17] Dimitry Tegunov and Patrick Cramer. Real-time cryo-em data pre-processing with warp. *bioRxiv*, 2018.
 - [18] L. A. Vese and C. L. Guyader. *Variational Methods in Image Processing*. Chapman & Hall/CRC Mathematical and Computational Imaging Sciences Series. CRC Press, 2015.
 - [19] Thorsten Wagner, Felipe Merino, Markus Stabrin, Toshio Moriya, Claudia Antoni, Amir Apelbaum, Philine Hagel, Oleg Sitsel, Tobias Raisch, Daniel Prumbaum, Dennis Quentin, Daniel Roderer, Sebastian Tacke, Birte Siebolds, Evelyn Schubert, Tanvir Shaikh, Pascal Lill, Christos Gatsogiannis, and Stefan Raunser. Sphire-cryolo: A fast and accurate fully automated particle picker for cryo-em. 2018.
 - [20] Feng Wang, Huichao Gong, Gaochao Liu, Meijing Li, Chuangye Yan, Tian Xia, Xueming Li, and Jianyang Zeng. DeepPicker: A deep learning approach for fully automated particle picking in cryo-em. *Journal of Structural Biology*, 195(3):325–336, 2016.
 - [21] Wilson Wong, Xiao-chen Bai, Alan Brown, Israel S. Fernandez, Eric Hanssen, Melanie Condron, Yan Hong Tan, Jake Baum, and Sjors H. W. Scheres. Cryo-em structure of the plasmodium falciparum 80s ribosome bound to the anti-protozoan drug emetine. *eLife*, 3, June 2014.
 - [22] Yanan Zhu, Qi Ouyang, and Youdong Mao. A deep convolutional neural network approach to single-particle recognition in cryo-electron microscopy. *arXiv e-prints*, art. arXiv:1605.05543, May 2016.